NMR Structural Studies Reveal a Novel Protein Fold for MerB, the Organomercurial Lyase Involved in the Bacterial Mercury Resistance System[†,‡]

Paola Di Lello,[§,||] Gregory C. Benison,[⊥] Homayoun Valafar,[#] Keith E. Pitts,[▽] Anne O. Summers,[▽,○] Pascale Legault,[*,§] and James G. Omichinski[*,§,⊥]

Departments of Biochemistry & Molecular Biology, Chemistry, and Microbiology, Southeast Collaboratory for Structural Genomics, and Center for Metalloenzyme Studies, University of Georgia, Athens, Georgia 30602, and Dipartimento di Scienze Ambientali, Seconda Università di Napoli, Via Arena 22, 81100 Caserta, Italy

Received February 12, 2004; Revised Manuscript Received May 4, 2004

ABSTRACT: Mercury resistant bacteria have developed a system of two enzymes (MerA and MerB), which allows them to efficiently detoxify both ionic and organomercurial compounds. The organomercurial lyase (MerB) catalyzes the protonolysis of the carbon−mercury bond resulting in the formation of ionic mercury and a reduced hydrocarbon. The ionic mercury [Hg(II)] is subsequently reduced to the less reactive elemental mercury [Hg(0)] by a specific mercuric reductase (MerA). To better understand MerB's unique enzymatic activity, we used nuclear magnetic resonance (NMR) spectroscopy to determine the structure of the free enzyme. MerB is characterized by a novel protein fold consisting of three noninteracting antiparallel β-sheets surrounded by six α-helices. By comparing the NMR data of free MerB and the MerB/Hg/DTT complex, we identified a set of residues that likely define a Hg/DTT binding site. These residues cluster around two cysteines (C^{96} and C^{159}) that are crucial to MerB's catalytic activity. A detailed analysis of the structure revealed the presence of an extensive hydrophobic groove adjacent to this Hg/DTT binding site. This extensive hydrophobic groove has the potential to interact with the hydrocarbon moiety of a wide variety of substrates and may explain the broad substrate specificity of MerB.

Mercury is present in the environment in a variety of chemical forms. It is highly toxic, and its toxicity depends on both the chemical form and the route of exposure. In the environment, mercury undergoes a complex biogeochemical cycle, and it is readily converted to inorganic salts and organomercurial compounds, such as methylmercury (MeHg), the most toxic form (*1*−*3*). The main source of MeHg in the environment is the enzymatic methylation of Hg(II),[1] a transformation that is mediated by methyl-cobalamine compounds present in microorganisms (*4*, *5*). This process takes place in rivers, lakes, and oceans where Hg(II) accumulates in the sediments from natural processes, like land erosion and atmospheric depositions, as well as anthropogenic activities (*6*, *7*). Because of its lipophilicity, MeHg easily enters the aquatic food chain where it is able to bioaccumulate to dangerously high levels.

Humans are exposed to MeHg almost entirely by consumption of contaminated fish and wildlife, which are at the top of the aquatic food chain. Once absorbed into the bloodstream, MeHg enters the blood cells where it binds to hemoglobin (*8*). From there, it can be transported to all tissues and several target organs such as the kidneys and liver. However, the critical organ for MeHg toxicity is the brain. It is believed that MeHg is able to pass through the blood−brain barrier via a MeHg−L-cysteine complex, which is transported by the L-amino acid carrier system (*9*). Because of its high affinity for sulfhydryl groups, MeHg can easily bind to thiol-containing molecules such as proteins, cysteine, and glutathione (*10*), causing alterations in essential biochemical processes (*11*−*13*).

Interestingly, mercury resistant bacteria have developed a detoxification system that allows them to survive in mercury-contaminated sites. The strategy adopted by these

[†] This work was supported by American Cancer Society Grant RPG LBC-100183 (J.G.O.) and a supplement (to J.G.O., P.L., and A.O.S.) to Grant 99ER62358 (to A.O.S.) from the Natural and Accelerated Bioremediation Research (NABIR) Program, Biological and Environmental Research (BER), Office of Science of the U.S. Department of Energy. P.D.L. was supported in part by a fellowship from the Second University of Naples. G.C.B. was a NSF Graduate Research Fellow.

[‡] Coordinates deposited to the Protein Data Bank with the code 1S6L.

* To whom correspondence should be addressed. Present address: Département de Biochimie, Université de Montréal, C. P. 6128 Succursale Centre-Ville, Montréal, Quebec H3C 3J7, Canada. Tel: 514-343-7341. J.G.O. E-mail: jg.omichinski@umontreal.ca. P.L. E-mail: pascale.legault@umontreal.ca.

[§] Department of Biochemistry & Molecular Biology, University of Georgia.

[||] Dipartimento di Scienze Ambientali, Seconda Università di Napoli.

[⊥] Department of Chemistry, University of Georgia.

[#] Southeast Collaboratory for Structural Genomics, University of Georgia.

[▽] Department of Microbiology, University of Georgia.

[○] Center for Metalloenzyme Studies, University of Georgia.

[1] Abbreviations: DSS, 2,2-dimethyl-2-silapentane-5-sulfonic acid; DTT, dithiothreitol; EDTA, ethylenediaminetetraacetic acid; Hg(0), elemental mercury; Hg(II), ionic mercury; HSQC, heteronuclear single quantum coherence spectroscopy; IPTG, isopropyl β-thiogalactoside; merbromin, (2,7-dibromo-9-(o-carboxyphenyl)-6-hydroxy-3-oxo-3H-xanthen-4-yl) hydroxymercury; mersalyl, 3-(hydroxymercuri)-2-methoxipropyl carbonyl phenoxyacetic acid; NMR, nuclear magnetic resonance; NOE, nuclear Overhauser enhancement; NOESY, nuclear Overhauser enhancement spectroscopy; PHMBA, *p*-(hydroxymercuri) benzoate; PHMSA, *p*-(hydroxymercuri) sulfonate; RDC, residual dipolar coupling; TAD, torsion angles dynamics; TOCSY, total correlation spectroscopy; TROSY, transverse relaxation optimized spectroscopy.

10.1021/bi049669z CCC: $27.50
Published on Web 06/12/2004

microorganisms consists in transforming toxic mercury-containing compounds, like organomercurials and inorganic mercuric salts, into Hg(0), which is hydrophobic, volatile, and less reactive with protein sulfhydryl groups (*14*, *15*). The bacterial resistance to mercury results from a series of proteins, which have specific roles in the detoxification pathway. The genes encoding these proteins are clustered in a plasmid-carried operon, and although the organization of the genes may vary in different bacteria, the common ones, found in all operons, are as follows: *merR*, *merA*, *merP*, and *merT*. The gene *merR* encodes a regulatory protein (MerR) that binds to the operator region of the *mer* operon repressing its own transcription and that of other *mer* genes (*15*). The genes *merP* and *merT* encode two proteins involved in transporting Hg(II) inside the cell (*15*−*17*). The *merA* gene product, a mercuric ion reductase, catalyzes the reduction of Hg(II) to the less toxic Hg(0), using NADPH as the source of electrons and FAD as a cofactor (*18*). Bacteria carrying this minimum set of four *mer* genes exhibit a narrow spectrum resistance; they can survive in the presence of mercuric ion compounds but not organomercurials (*15*, *19*). Some bacteria carry an additional gene, *merB*, encoding for an organomercurial lyase that gives them resistance to organomercurial compounds. These bacteria are usually referred to as "broad spectrum", because they are resistant to a broad variety of organic and inorganic mercury compounds (*15*, *19*).

MerB is a unique enzyme that catalyzes the protonolysis of the carbon−mercury bond in organomercurials, yielding an aliphatic or aromatic compound and Hg(II) (*20*). Hg(II) can then be reduced to Hg(0) by the specific reductase MerA. MerB shows a broad substrate specificity, and it can cleave a large variety of organomercurial compounds ranging from simple alkyl compounds such as MeHg to polyaromatic heterocyclic compounds such as merbromin (*20*, *21*). MerB displays different turnover rates (0.7−240 min^{-1}) for various substrates, but in general, it has a slight preference for aryl mercurials (for more details, see refs *20* and *21*). On the basis of extensive mechanistic studies, Walsh and coworkers proposed a bimolecular electrophilic substitution (S_E2) mechanism for the reaction catalyzed by MerB and have demonstrated that this reaction is dependent on the presence of thiols in the buffer (*21*). In addition, the importance of the conserved cysteine residues in MerB for its activity has been clearly demonstrated in mutational studies (*22*). Despite the kinetic studies on this unique enzyme, the structural features that allow MerB to bind organomercurials and release Hg(II) remain unknown. To date, no three-dimensional (3D) structure is available for MerB, and there is no information about the amino acid residues, other than cysteines, that form the organomercurial-binding site.

We have determined the 3D structure of MerB in the free form by NMR spectroscopy. We have found that MerB adopts a novel protein fold characterized by three noninteracting antiparallel β-sheets surrounded by six α-helices. We initially used NMR chemical shift mapping to study the interaction of MerB with various organomercurial substrates in the presence of DTT. Interestingly, the exposure of MerB to all organomercurials tested in the presence of DTT resulted in the formation of a stable MerB/Hg/DTT complex. The comparison of two-dimensional (2D) $^1H-^{15}N$ HSQC spectra of free MerB and the MerB/Hg/DTT complex allowed us to identify residues that likely form the Hg/DTT binding site. Analysis of the MerB structure revealed that functionally important cysteines are located within this Hg/DTT binding site. In addition, we identified a large hydrophobic groove adjacent to this Hg/DTT binding site. We propose that this hydrophobic groove is in the position to interact with the hydrocarbon portion of the substrate. This NMR investigation helps to explain the broad substrate specificity of this unique enzyme and provides insights into the structural framework for MerB catalysis.

EXPERIMENTAL PROCEDURES

Protein Expression and Purification. The *merB* gene from plasmid R831b (*23*) was amplified by polymerase chain reaction, and the NdeI/XhoI fragment was ligated into the expression vector pET21b (Novagen). The resulting plasmid was identical to pQZB1 except for the insertion of a stop codon between the XhoI site and the MerB-encoding sequence (*22*). This construct prevented the fusion to MerB of the polyhistidine tag present in pQZB1. The protein was overexpressed in the host bacterial strain BL21(DE3). Uniformly ^{15}N and $^{13}C/^{15}N$-labeled MerB were obtained by growing the host cells in modified M9 minimal media containing ^{15}N-labeled NH_4Cl (18.4 mM) and glucose or ^{13}C-labeled glucose (13.4 mM) as the sole nitrogen and carbon sources, respectively; IPTG at a concentration of 21 μM was used to induce the expression continuously. Each liter of minimal medium was inoculated with 1 mL of an LB starter culture grown at 37 °C for ∼5 h. The bacteria in minimal media were grown overnight at 37 °C. The cells were harvested by centrifugation and then kept frozen at −80 °C until further use.

For the protein purification, the cells were suspended in ∼100 mL of a buffer (25 mM Tris, pH 8.0, 1 mM EDTA, 2 mM DTT, and 5 mM benzamidine). The suspended cells were lysed by two passages through a French press, and the resulting lysate was cleared by centrifugation at 105,000*g* and 4 °C for 1 h. The supernatant from the cleared lysate was passed through a DEAE-Sepharose (Amersham Biosciences) column (50 mm i.d. × 40 cm length). The column (300 mL resin volume) was first equilibrated with buffer A (25 mM Tris, pH 8.0, 1 mM EDTA, and 2 mM DTT), and then, the protein was eluted using a linear gradient (0−100% over 1800 mL) of buffer B (buffer A + 1 M NaCl). The fractions containing MerB were pooled and dialyzed overnight into buffer C (20 mM sodium phosphate, pH 7.2, 1 mM EDTA, and 1 mM DTT) and applied to a Q-Sepharose (Amersham Biosciences) column (26 mm i.d. × 40 cm length) equilibrated with buffer C. The protein was eluted from the column (100 mL resin volume) using a linear gradient (0−100% over 1050 mL) of buffer D (buffer C + 1 M NaCl). Fractions containing the enzyme were pooled and dialyzed overnight against buffer E (20 mM sodium phosphate, pH 7.5, 1 mM DTT, 1 mM EDTA, and 100 mM NaCl). Following overnight dialysis, the sample was concentrated to ∼15 mL using an Amicon stirred-cell equipped with a 10K cutoff membrane (Millipore). The protein solution was then loaded in 500 μL aliquots onto a Superose 12 HR 10/30 column (Amersham Biosciences), previously equilibrated with buffer E. For each chromatographic cycle, the protein was eluted with 30 mL of the same buffer. The fractions containing the purified MerB protein were pooled

and dialyzed into the final NMR buffer (10 mM sodium phosphate, pH 7.5, 10 mM NaCl, 7.5 mM DTT, and 1 mM EDTA).

Preparation of NMR Samples. The samples for NMR studies contained 1.0−1.5 mM MerB (^{15}N- or ^{15}N/^{13}C-labeled) in NMR buffer and 90% H_2O/10% D_2O or 99.9% D_2O (Isotec Inc.). For measurements of RDCs, the protein was oriented using Pf1 phages as described by Pardi and coworkers (*24*). Pf1 phages (ASLA) were used at a concentration of ∼11 mg/mL corresponding to a ^{2}H quadrupolar splitting of 10.5 Hz. NMR samples of the MerB/Hg/DTT complex were prepared by titrating 1 equiv of an organomercurial substrate (mersalyl, merbromin, PHMBA, or PHMSA from Aldrich) into a prepared MerB sample containing either L-DTT (Sigma) or racemic DTT (Inalco).

NMR Spectroscopy. All NMR spectra were collected at 300 K on Varian Unity Inova 600 and 800 MHz spectrometers equipped with *z* pulsed-field gradient units and triple resonance HCN probes. For experiments involving amide proton detection in the direct dimension, the pulsed-field gradient-enhanced sensitivity approach was used (*25*), and ^{15}N decoupling during acquisition was achieved with the WALTZ16 scheme using a 1 kHz B_1 field (*26*). For experiments that detected aliphatic protons in the direct dimension, the GARP1 sequence was used for ^{13}C decoupling during acquisition (*27*). Either WATERGATE (*28*) or water flip-back pulse (*29*) trains were used to suppress the water signal. Quadrature detection was achieved using the States-TPPI method. The backbone and aliphatic side chain resonances of MerB (^{1}H, ^{15}N, and ^{13}C) were assigned using a combination of experiments as previously described (*30*). Distance restraints were obtained from the following experiments: 3D ^{15}N-edited NOESY-HSQC (with 80 ms mixing time) (*31*, *32*), 3D ^{13}C-edited HMQC-NOESY (with 40 ms of mixing time) (*33*), and four-dimensional (4D) ^{13}C/^{13}C-edited HMQC-NOESY-HMQC (with 90 ms mixing time) (*34*, *35*).

The coupling constants $^3J_{HNH_\alpha}$ were determined from the ratio between the intensities of crosspeaks and diagonal peaks in the HNHA experiment (*36*), according to the equation:

$$I_{cross}/I_{diag} = -\tan^2(2\pi^3 J_{HNH_\alpha}\zeta)$$

The error in the *J* coupling, caused by relaxation effects, was corrected by multiplying the measured coupling by 1.11 (*36*). Heteronuclear ^{15}N−^{1}H steady-state NOEs were measured using the pulse sequence reported by Kay and coworkers (*37*). A set of two spectra was recorded with (NOE experiment) and without (no NOE experiment) the use of a ^{1}H saturation period of 3 s applied before the start of the experiment. ^{1}H saturation consisted of a series of 120° pulses applied every 5 ms. In the spectrum with ^{1}H saturation, a 3 s recycling delay was applied before the saturation period. For the spectrum without ^{1}H saturation, a total recycling delay of 6 s was used. One-bond ^{1}H−^{15}N RDCs ($^1D_{NH}$) were measured from the difference between the splitting observed under anisotropic conditions and the splitting observed under isotropic conditions in the ^{15}N indirect dimension of IPAP−^{1}H−^{15}N HSQC spectra (*38*). One-bond $^{13}C^\alpha$−$^{13}C'$, ^{15}N−$^{13}C'$ ($^1D_{C\alpha C'}$ and $^1D_{NC'}$), and additional ^{1}H−^{15}N dipolar couplings were determined from TROSY-based HNCO experiments (*39*); one-bond dipolar couplings $^{13}C^\alpha$−$^{13}C'$ and ^{15}N−$^{13}C'$ were normalized to the $^1D_{NH}$ coupling constants by multiplying each observed constant by the appropriate scaling factor: 5.0 for $^1D_{C\alpha C}$ and 8.3 for $^1D_{NC'}$ (*40*). Errors in the measurements were estimated to be 1−2 Hz depending on the line shape of the signals (*40*). NMR data were processed using the NMRPipe/NMRDraw package (*41*) and analyzed with PIPP (*42*) and NMRView (*43*).

Structure Calculations. The interproton distances were estimated from the intensities of the cross peaks observed in the 3D ^{15}N-edited NOESY-HSQC (*31*, *32*), 3D ^{13}C-edited HMQC-NOESY (*33*), and 4D ^{13}C/^{13}C-edited HMQC-NOESY-HMQC (*34*, *35*) experiments. The NOE intensities were classified into three distance ranges, defined as strong (1.8−2.8 Å), medium (1.8−3.4 Å), and weak (1.8−5.0 Å), by comparison with known short distances (<5 Å) in elements of regular secondary structures of the protein (d_{NN} and $d_{\alpha\beta(i,i+3)}$ for the α-helices 39−46, 50−58, and 168−176). The upper bounds for distance restraints involving equivalent or nonstereospecifically assigned protons were corrected using the r^{-6} averaging approach, as suggested by Neuhaus and coworkers (*44*). The backbone dihedral angles were obtained from the analysis of $^1H^\alpha$, ^{15}N,$^{13}C'$, $^{13}C^\alpha$, and $^{13}C^\beta$ chemical shifts using the program TALOS (*45*). The average values of φ and ψ predicted by the program were used as experimental restraints with an error set to $\pm 1.5\sigma$ (where σ was the standard deviation calculated by TALOS for each φ and ψ value) or at least ±15°. For some residues, the values of φ and ψ predicted by TALOS could not be considered reliable; in these cases, when the value for the coupling constant $^3J_{HNH_\alpha}$ was available from analysis of the HNHA experiment, angle restraints φ were derived from the Karplus curve (*46*). Additional ψ angles were estimated based on the ratio $d_{N\alpha}$ (*i*, *i*) NOE/$d_{\alpha N}$ (*i* − 1, *i*) NOE and the chemical shift index (CSI) (*47*, *48*): residues falling in the β-sheet region of the Ramachandran plot are characterized by a ratio $d_{N\alpha}/d_{\alpha N} < 1$ while residues in the right-handed α-helix region have a $d_{N\alpha}/d_{\alpha N} > 1$ (*49*). Considering that this ratio depends on the ψ angle of residue $i - 1$, values of $\psi = 130 \pm 90°$ and $\psi = -45 \pm 35°$ were used for $d_{N\alpha}/d_{\alpha N} < 1$ and $d_{N\alpha}/d_{\alpha N} > 1$, respectively. Amide protons in slow exchange with the solvent were identified by recording a 2D ^{1}H−^{15}N HSQC of MerB exchanged in D_2O. The hydrogen bonds were defined as restraints for the slowly exchanging amide protons only after the initial rounds of calculation had revealed the fold of the protein and only for those amide protons whose acceptor could be easily identified based on the preliminary structure. The hydrogen bond distance restraints were used for ^{1}H−O (1.3−2.5 Å) and for N_H−O (2.3−3.5 Å). The values for the rhombicity *R* and the axial component D_a of the alignment tensor were estimated using the maximum likelihood method (*50*). To optimize the value of both of these parameters, a set of preliminary calculations was run using a "grid search" approach (*51*) with *R* varying in the range of 0.1−0.7 Hz (in step of 0.1) and D_a varying between 18.3 and 10.2 Hz.

Structure calculations were performed with the program CNS (*52*) using a combination of TAD and Cartesian dynamics (*53*). A modified version of the simulated annealing protocol was used to introduce RDCs ($^1D_{NH}$, $^1D_{C_\alpha C}$, and $^1D_{NC'}$) in the structure calculations (*54*). As discussed by Kay and coworkers (*54*), the standard torsion angle molecular dynamics methodology in CNS needs to be modified when

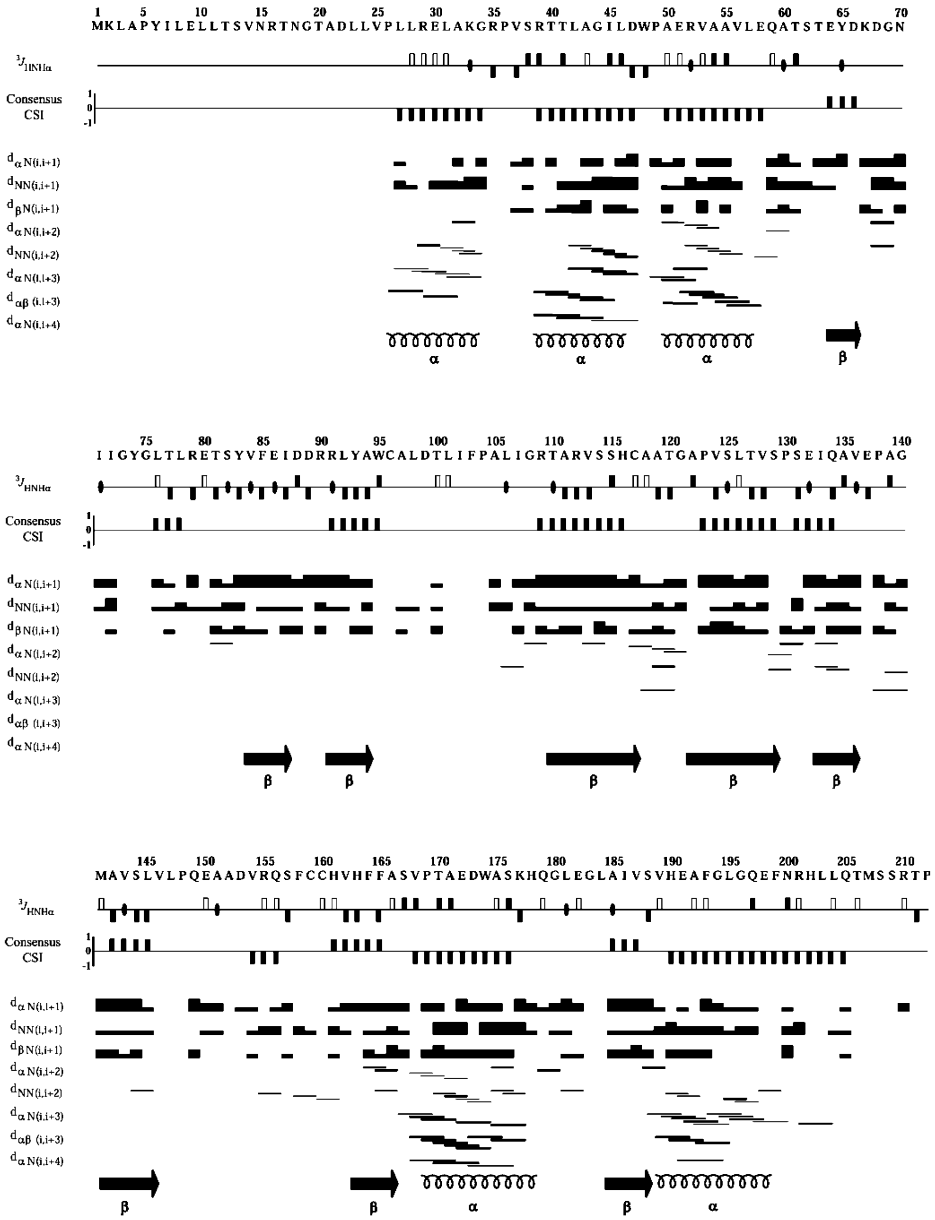

FIGURE 1: Secondary structure of MerB from NOE, $^3J_{HNH_\alpha}$ couplings, and chemical shift data. Sequential and medium-range NOEs were observed for MerB at 300 K and pH 7.5 in the ^{15}N-edited NOESY−HSQC and 3D ^{13}C-edited HMQC−NOESY spectra, collected with mixing times of 80 and 40 ms, respectively. The thickness of the bars representing the NOEs is proportional to the intensity of the signals. For the coupling constants $^3J_{HNH_\alpha}$, downward filled boxes correspond to $J \geq 8$ Hz, upward filled boxes indicate $J \leq 6$ Hz, and filled ovals are used for 6 Hz $\leq J \leq$ 8 Hz. Upward blank boxes indicate residues for which no cross peak was detectable in the HNHA experiment. Coupling constants not estimated because of resonance overlap are indicated by a dash. Consensus CSI values of −1 indicate an α-helix conformation, whereas values of 1 correspond to β-strand structures.

applied to structure calculations of proteins with high molecular weights, using a limited number of NOEs in combination with RDC constraints. Therefore, as suggested, we used a much longer slow-cooling TAD period and optimized values of the force constant for RDC restraints, and smaller values of the time steps were employed during the molecular dynamics trajectory. Starting from an extended structure with standard geometry, 50 structures were calculated using NOE-derived interproton distances, dihedral angles (ϕ, ψ, and χ), hydrogen bond-derived distances, and one-bond dipolar couplings $^1D_{NH}$, $^1D_{C_\alpha C'}$, and $^1D_{NC'}$. These 50 structures contained no NOE violation greater than 0.3 Å and no backbone dihedral angle restraint violation greater than 2°. From this set of 50 structures, the 20 structures with the lowest energies were selected for further analysis. The quality of the structures was analyzed using the programs PROCHECK-NMR (*55*), MOLMOL (*56*), and PROMOTIF (*57*). All of the figures representing the structures were generated using the program MOLMOL.

RESULTS AND DISCUSSIONS

Secondary Structure. The secondary structure of MerB was initially predicted by the CSI (*47*, *48*), based on the chemical shifts for the $^1H^\alpha$, $^{13}C^\alpha$, $^{13}C'$, and $^{13}C^\beta$ nuclei (Figure 1). The CSI method predicted six α-helices and nine β-strands. The CSI predictions were generally in agreement with the NOE patterns observed in the ^{15}N-edited and ^{13}C-edited NOESY spectra (Figure 1). The NOE patterns defined three α-helices at the amino terminus between residues 26−33 (α1), 39−46 (α2), and 50−58 (α3), a fourth α-helix between residues

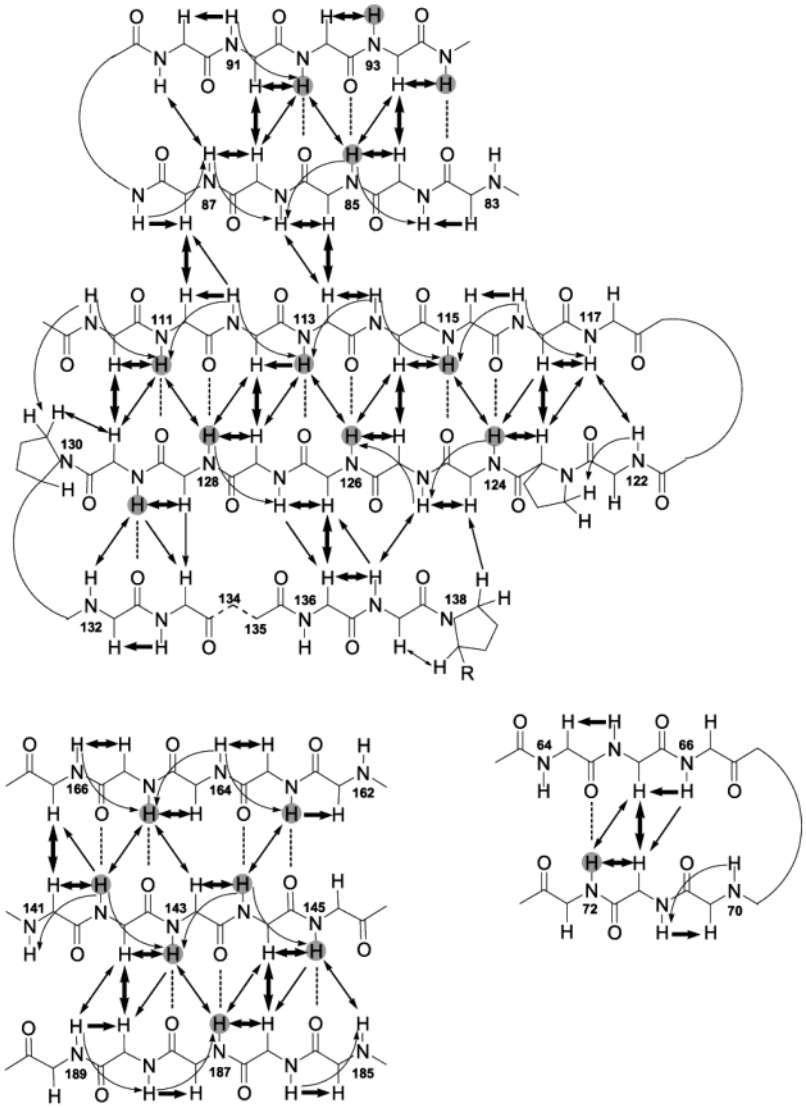

FIGURE 2: Sequential and long-range NOEs observed for the antiparallel β-sheets of MerB at 300 K and pH 7.5. Thick arrows indicate strong NOEs connectivities while thin arrows indicate medium to weak NOEs. The slowly exchanging amide protons are shaded in gray. The dashed lines indicate the 18 hydrogen bonds included in the structure calculations.

168−176 (α4), and a long helix at the carboxyl terminus (α5). For the sixth α-helix predicted by the CSI (residues 155−157), only medium to weak sequential d_{NN} and some medium-range $d_{NN(i,i+2)}$ NOEs were observed. Even though the ΔH^{α} and ΔC^{α} secondary shifts and the TALOS prediction were consistent with an α-helix, the NOE pattern of this type of secondary structure was not observed. This may indicate a conformational heterogeneity for this region. Also in agreement with the CSI prediction, the sequential and medium-range NOE connectivities observed in the regions between residues 83−87, 90−94, 110−116, 123−129, 132−137, 141−145, 162−165, and 185−188 suggested the presence of β-strand elements. The presence of these β-strands was also confirmed by the observation of long-range NOEs between residues of adjacent strands.

A schematic representation of the NOE connectivities for the β-sheet structures in MerB is shown in Figure 2. The pattern of long-range $d_{\alpha\alpha(i,j)}$, $d_{\alpha N(i,j)}$, and $d_{NN(i,j)}$ NOEs indicated that the β-strands were organized in three separate antiparallel β-sheets. The major β-sheet structure comprised the strands between residues 83−87, 90−94, 110−117, 122−130, and 132−137; a second one included the three strands constituted by residues 163−166, 141−145, and 185−189; and the smallest one involved residues 65−66 and 70−71. The presence of hydrogen bonds in the β-sheets was confirmed by the slow exchange rate of the involved amide protons in the 2D $^{1}H-^{15}N$ HSQC spectrum of the uniformly ^{15}N-labeled MerB in D_2O. This experiment was collected 1 week after the sample had been exchanged from a 90% H_2O/10% D_2O solution to 100% D_2O solution; many amide protons were still detectable (data not shown), and the majority of them were from residues in the β-sheet regions of MerB. These hydrogen bonds were used as additional constraints in the final run of the structure calculations.

Three-Dimensional Structure of MerB. The 3D structure of MerB was determined using a set of 1493 NOE-derived distance restraints, 203 ϕ and ψ dihedral angle restraints, five χ angle restraints, 36 hydrogen bond restraints, and 298 one-bond RDC restraints ($^{1}D_{NH}$, $^{1}D_{C\alpha C'}$, and $^{1}D_{NC'}$). There were 556 intraresidue NOEs, 678 sequential, short-range, and medium-range ($|i - j| \leq 4$) NOEs, and 259 long-range ($|i - j| > 4$) NOEs (Table 1). The side chain torsion angles

Table 1

Restraints used for the structure calculations	
total NOE distance restraints	1493
intraresidue	556
sequential ($\|i - j\| \leq 4$)	678
long-range ($\|i - j\| > 4$)	259
hydrogen bonds	36
dihedral angle restraints (ϕ, ψ, χ)	208
RDC restraints ($^1D_{NH}$, $^1D_{C\alpha C'}$, and $^1D_{NC'}$)	298
Structural statistics	
RMSDs from idealized geometry	
bonds (Å)	0.0029 ± 0.00003
angles (deg)	0.4038 ± 0.0039
impropers (deg)	0.3073 ± 0.0057
RMSD from distance restraints (Å)	0.0285 ± 0.0004
RMSD from dihedral restraints (deg)	0.275 ± 0.019
RMS difference from RDC restraints (Hz)[a]	
$^1D_{NH}$	2.90 ± 0.10
$^1D_{NC'}$	3.24 ± 0.06
$^1D_{C\alpha C'}$	5.50 ± 0.07
Procheck statistics (%)	
residues in most favored regions	76.3
residues in additional allowed regions	18.0
residues in generously allowed regions	3.6
residues in disallowed regions	2.1
Atomic pairwise RMSD (Å) for backbone atoms (C′, C$^\alpha$, and N)	
global[b]	1.26 ± 0.35
N-terminal region[c]	0.70 ± 0.20
core region[d]	0.61 ± 0.14
Atomic pairwise RMSD (Å) for all heavy atoms	
global[b]	1.87 ± 0.28
N-terminal region[c]	1.64 ± 0.18
core region[d]	1.39 ± 0.13

[a] Mean value, over the 20 lowest energy structures, of the root-mean-square difference between the measured and the calculated values of the RDCs. [b] Only residues 26−58, 64−72, 83−94, 105−145, 162−177, and 185−202 were used for the RMSD calculation. [c] Only residues 26−58 and 64−72 were included in the RMSD calculation. [d] Only residues 83−94, 105−145, 162−177, and 185−202 were included in the RMSD calculation.

χ were for Val[84], Val[113], Val[128], Val[136], and Val[143]. The 36 hydrogen bond restraints were derived from the slowly exchanging amide protons.

Structure calculations were performed using the torsion angle molecular dynamics protocol of CNS, starting from an extended structure. The first 20 amino acids of the disordered amino terminus were not included in the calculations (*30*). From the 55 calculated structures, 50 were accepted because they had no upper bound violation greater than 0.3 Å and no dihedral angle restraint violation greater than 2°. From this set of accepted structures, the 20 structures with the lowest energies were selected for further analysis. All of the structures in the ensemble had good covalent geometry as shown by small deviations from the idealized geometry (Table 1). On the basis of the Ramachandran plot analysis in PROCHECK-NMR, 98% of ϕ and ψ dihedral angles were within the allowed regions, whereas 2% of the amino acids had unfavorable backbone conformations. The residues in disallowed regions are mainly glycines and amino acids located in loops or in less well-defined portions of the protein. Structural statistics for the ensemble of the 20 lowest energy structures of MerB are reported in Table 1.

On the basis of the NMR data, MerB adopts a 3D structure characterized by six α-helices and three separate antiparallel β-sheets (Figure 3A). Three α-helices are located at the amino terminus of the protein between residues 26−32 (α1),

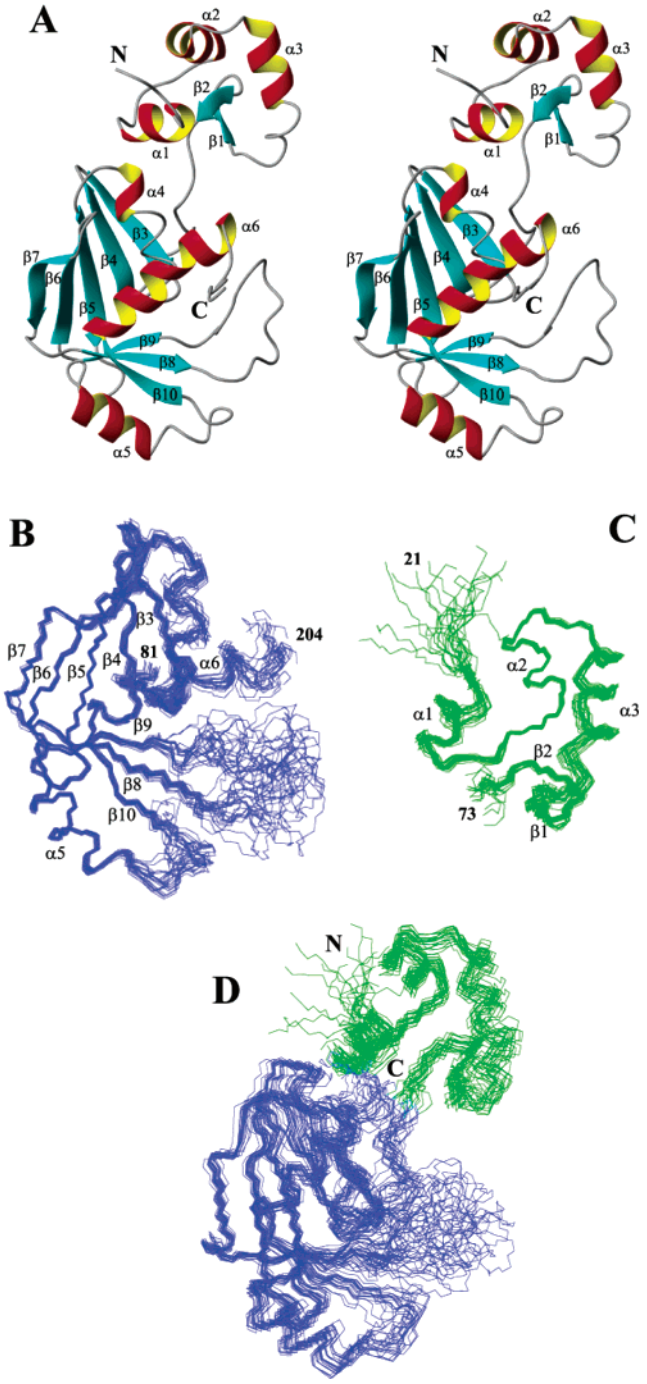

FIGURE 3: (A) Stereoview of the ribbon model of one representative structure of MerB from the ensemble of the 20 lowest energy structures. (B−D) Overlay of the 20 lowest energy structures. The structures were superimposed using the backbone atoms C′, C$^\alpha$, and N. Superimposition of (B) the core of the protein (residues 83−94, 105−145, 162−177, and 185−202), (C) the amino-terminal region (residues 26−58 and 64−72), and (D) the full protein (residues 26−58, 64−72, 83−94, 105−145, 162−177, and 185−202).

39−46 (α2), and 50−58 (α3), and they are followed by a short and highly twisted β-sheet (sheet A) involving residues 65−66 (β1) and 70−71 (β2). The α1 and α2 helices are connected by a six residue loop (33−38), whereas a three residue linker (47−49) connects α2 and α3. The two short strands β1 and β2 are connected through a β-turn of type II′, which is stabilized by a hydrogen bond involving the amide proton of Gly[69] and the carbonyl of Asp[66]. The short

β-sheet is packed against loop 33−38, with residues from strand β2 facing the loop and making interactions with Val[37], Ser[38], and Arg[39]. The $\alpha\alpha\alpha\beta\beta$ topology that characterizes the amino-terminal region of MerB is stabilized by a number of hydrophobic interactions between the side chains of α1 (Pro[26], Glu[30]) and α2 (Thr[41], Ile[45], and Leu[46]) and between the side chains of α2 (Ala[43], Trp[48]) and α3 (Ala[50], Val[53]).

A second, five-stranded β-sheet (sheet B) is comprised of residues 83−87 (β3), 90−94 (β4), 111−116 (β5), 123−128 (β6), and 133−137 (β7). This sheet contains a bulge involving residues 133−135, which creates a distortion in the outer strand β7. The two strands β3 and β4 are connected by a tight turn of type IV (residues 87−90), stabilized by a hydrogen bond between the amide proton of Arg[90] and the carbonyl of Ile[87]; two consecutive type IV turns, involving residues 117−120 and 118−121, link the strands β5 and β6, whereas a type I β-turn connects strand β6 to β7.

Three shorter strands, β8 (residues 142−145), β9 (residues 163−165), and β10 (residues 185−188), form the third antiparallel β-sheet (sheet C). The two major β-sheets (B and C) are oriented almost perpendicular to each other, and this orientation is stabilized by hydrophobic interactions between residues from β5 (Val[113] and Ser[115]), β6 (Val[124] and Leu[126]), and β9 (Phe[164]). The fifth α-helix (α5), formed by residues 168−176, packs against the three-stranded β-sheet (sheet C), and several of its hydrophobic residues (Val[168], Ala[171], and Ala[175]) interact with side chains from β8 (Ala[142]), β9 (Phe[165]), and β10 (Ile[186] and Ser[188]) and with the region 117−122 that connects the strand β5 to β6. The side chains of residues from β8, β9, and β10 are involved in hydrophobic interactions on both sides of the three-stranded β-sheet, with β5/β6 on one side and with α5 and the loop 117−122 on the other side; such interactions define the hydrophobic core of the protein. The sixth α-helix (α6) is located at the carboxyl terminus of the protein, and it extends between residues 189 and 204.

The less well-defined regions of the protein are between residues 73−82, 95−104, 146−161, and 178−184. The regions 73−82 and 95−104 are not well-defined in the calculated structures due to the incomplete resonance assignment of several residues and because of the limited number of unambiguously assigned NOEs in the region. However, both the CSI prediction and the amide exchange data suggest that these regions are structured. The consensus CSI predicted a β-strand, involving residues 76−78 (Figure 2), and the hydrogen−deuterium exchange data (data not shown) showed that Ile[72], Gly[73], Leu[76], Thr[77], Thr[100], and Leu[101] are protected from exchange with the solvent. These results are supported by the ^{15}N−^{1}H heteronuclear NOE data. For the majority of the residues in these two regions, the values of the ^{15}N−^{1}H NOE (Figure 4) are within one standard deviation from the average, indicating the absence of backbone flexibility on fast time scales (picoseconds to nanoseconds).

In contrast, the long loop between Val[146] and His[161] appears to be very flexible with the exception of a few residues (Asp[153], Arg[155], Ser[157], and Cys[159]). All of the amino acids in this region have ^{15}N−^{1}H heteronuclear NOE values more than one standard deviation below the average (Figure 4). The same is observed for Gly[180], Leu[181], Glu[182], and Gly[183] in the loop formed by residues 178−184 and for several amino acids at the carboxyl terminus.

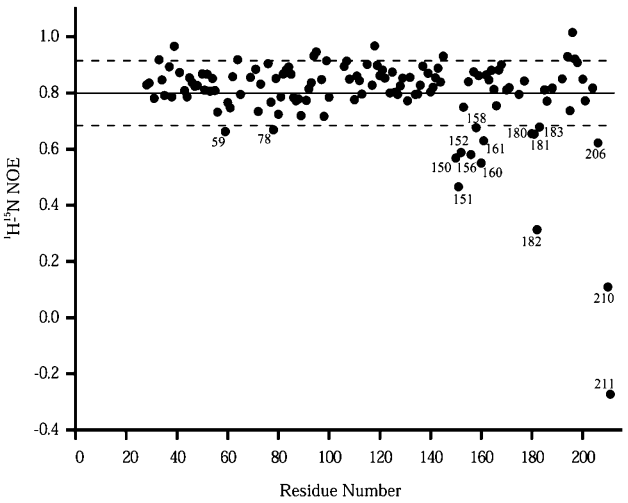

FIGURE 4: Plot of the heteronuclear ^{15}N−^{1}H NOEs for MerB. The horizontal dashed lines correspond to the mean value ± σ (0.80 ± 0.11). The average ^{15}N−^{1}H NOE (solid line) has been calculated excluding the negative value of Thr[211].

Overall, MerB adopts a well-defined fold between Pro[26] and Leu[204]. The backbone superimpositions of the 20 lowest energy NMR structures are reported in Figure 3B−D; for clarity, residues 1−20, at the disordered amino terminus, and residues 205−212, at the disordered carboxyl terminus, are not shown. Excluding the disordered loops (residues 146−161 and 178−184) and the less well-defined regions (residues 73−82 and 95−104), both the amino terminus (residues 26−72) and the core of the protein (residues 83−202) are individually precisely defined (Figure 3B,C). The pairwise RMSD for the ensemble of the 20 lowest energy structures, in the regions 83−94, 105−145, 162−177, and 185−202, is 0.61 ± 0.14 Å for the backbone atoms and 1.39 ± 0.13 Å for all of the heavy atoms, whereas for residues 26−58 and 64−72 the pairwise RMSD is 0.70 ± 0.20 Å for the backbone atoms and 1.64 ± 0.18 Å for the heavy atoms.

The amino-terminal region (residues 26−72), although well-characterized within the local elements of secondary structure, is less precisely defined with respect to the rest of the protein (Figure 3D). This is due to the limited number of unambiguously assigned medium- and long-range NOEs involving this region and the core of the protein. As a consequence, the global pairwise RMSD for residues 26−58, 64−72, 83−94, 105−145, 162−177, and 185−202 rises to 1.26 ± 0.35 Å for the backbone atoms and 1.87 ± 0.28 Å for all of the heavy atoms.

The Structure of MerB Is Unique. It is important to point out that the NMR-derived structure of MerB does not seem homologous to any other known fold in the Protein Data Bank. An extensive search in the structural database, using the Dali method (*58*) (www.ebi.ac.uk/dali), did not produce any significant matches. In some cases, a particular arrangement of a few elements of secondary structure was recognized in proteins with known structures, but no protein was found to have an overall fold similar to MerB. Interestingly, among all of the proteins that were found to have a similarity with MerB, the most recognized motif was the $\alpha\alpha\alpha\beta\beta$ arrangement present in the amino-terminal region of MerB. Such an arrangement shows the typical feature of the well-known winged helix fold, which is involved not only in

sequence specific DNA binding, but it has also been shown to mediate protein−protein interactions (*59*).

The Role of Cysteines in MerB Structure and Function. Early studies on the function of MerB showed that the cysteine residues present in the sequence were important for the enzymatic activity. MerB from *Escherichia coli* (R831b) has four cysteines, Cys[96], Cys[117], Cys[159], and Cys[160], but only three of them (Cys[96], Cys[117], and Cys[159]) are highly conserved. Site-directed mutagenesis of any of these four individual cysteines to alanine caused a loss of resistance to organomercurials, suggesting that all of the four cysteines play an important role in MerB's activity (*60*). Recently, the enzymatic activity of single mutants in which each individual cysteine residue had been changed to a serine has been characterized (*22*). These studies showed that the C96S and C159S mutations lead to a complete loss of enzymatic activity, whereas the C160S mutation results in the retention of about 37% of the wild-type activity. The enzymatic activity of the C117S mutant could not be assessed because of its tendency to form insoluble precipitates.

Now that the structure of MerB has been determined, it is interesting to analyze the position of the four cysteines within the 3D structure of the enzyme. The highly conserved Cys[117] is positioned in the core of the protein, whereas the other three cysteines Cys[96], Cys[159], and Cys[160] are solvent exposed (Figure 5A). Cys[117] is protected from the solvent by the side chains of Ala[119], Thr[120], Ala[122], Ala[166], and Thr[170], and it is prevented from interacting with the other three cysteines by the side chains of Ala[118] and Phe[165] (Figure 5B). These structural features confirm the hypothesis that Cys[117] has primarily a structural role (*22*). Any involvement of Cys[117] in the protonolysis reaction, as activating ligand and/or proton donor, has to be excluded because its side chain is completely buried in the hydrophobic core of the enzyme. The other three cysteines (Cys[96], Cys[159], and Cys[160]) are very close in 3D space, and this is in agreement with the results that at least two of them are involved in cleavage of the carbon−mercury bond (*21*, *22*). Cys[159] and Cys[160] are in a region of the structure that is predicted to be α-helical by the CSI, but the characteristic NOEs pattern of this type of secondary structure is not observed in the NMR data, except for some weak $d_{NN(i,i+2)}$. This may suggest that an α-helical conformation is partially populated and in conformational exchange with an alternative conformation. The $^{15}N-^{1}H$ heteronuclear NOE relaxation data could support such an explanation. In fact, residues Arg[155], Ser[157], and Cys[159] show high values of the $^{15}N-^{1}H$ NOEs (Figure 4). As observed for Cys[159] and Cys[160], Cys[96] is also in a region of the protein that is not well defined by the NMR data. In the 2D $^{1}H-^{15}N$ HSQC, the amide peak for this cysteine was not observed either because it is exposed and in fast exchange with the solvent or because of internal mobility that causes a severe broadening of the signal. Therefore, the three critical cysteines appear to have an intrinsic flexibility. This flexibility could help to explain the reactivity of MerB toward a broad spectrum of organomercurial substrates. Alternatively, some or all of the cysteines in this region (Cys[96], Cys[159], and Cys[160]) could be stabilized by the presence of mercury.

Location of a Hg/DTT Binding Site in MerB. To gain a better insight on the location of the organomercurial-binding site, NMR experiments examining the interactions of MerB with several organomercurial substrates were performed (*61*).

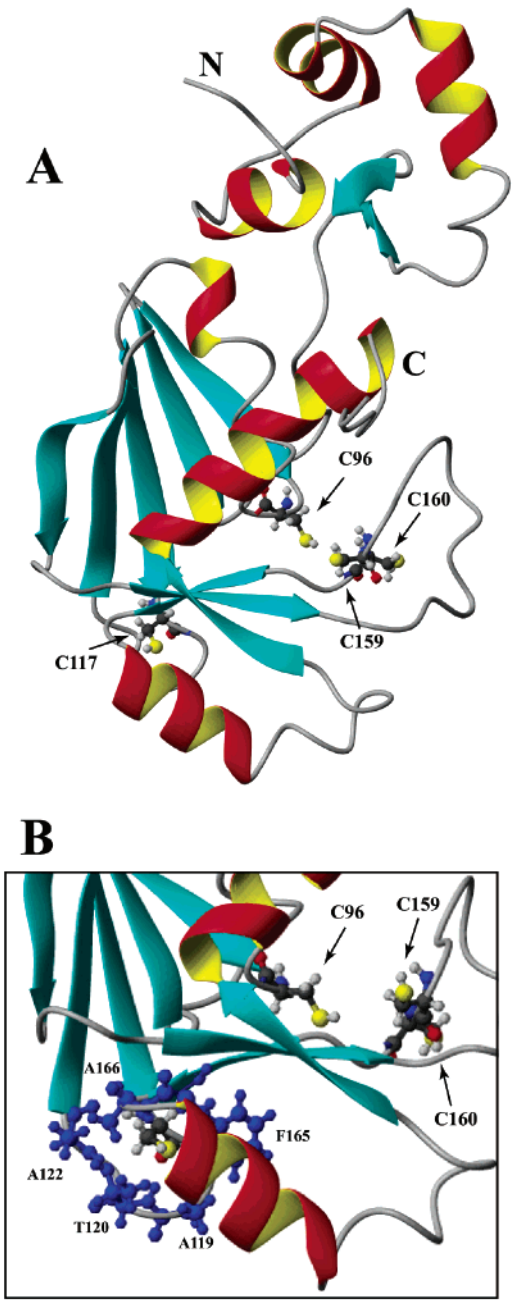

FIGURE 5: Ribbon model of a representative structure of MerB highlighting the position of the four cysteines. Three (Cys[96], Cys[159], and Cys[160]) of the four cysteines in the protein are close in space and solvent-exposed (A) whereas Cys[117] is buried in the hydrophobic core of the protein (B).

We observed that the 2D $^{1}H-^{15}N$ HSQC spectra of ^{15}N-labeled MerB upon exposure to various organomercurial substrates displayed numerous significant chemical shift changes when compared with free MerB (*30*). Interestingly, the spectra were identical regardless of the substrate added, and several signals were observed as pairs of peaks with similar ^{1}H and ^{15}N chemical shifts (*61*). The explanation for these results was due to the addition of DTT to the sample preparation. In the system studied, the enzyme cleaves the activated carbon−mercury bond of the substrate, and a Hg−DTT intermediate remains bound to MerB (*61*). DTT (1,4 dimercapto-2,3 butanediol) is a mixture of two enantiomers (*R*,*R* and *S*,*S*), so when the Hg−DTT intermediate is bound to the optically active protein, it forms two diastereomers

(MerB/Hg/*R*,*R*-DTT and MerB/Hg/*S*,*S*-DTT). The two diastereomers give rise to pairs of peaks in the 2D $^{1}H-^{15}N$ HSQC spectrum for those residues that are in the vicinity of the bound DTT.

Interestingly, many of the residues that experience a significant change in ^{1}H, ^{15}N, and C′ chemical shifts upon formation of the MerB/Hg/DTT complex also give rise to two amide signals in the diastereomeric complexes. If the residues displaying significant chemical shift changes between the free and the bound form are mapped on the 3D structure of free MerB (Figure 6A), they are spatially in proximity to each other. The residues experiencing the most significant changes in the chemical shifts of ^{1}H, ^{15}N, and C′ belonged to three regions of the protein sequence, centered around Leu^{76}, Cys^{96}, and Cys^{160} (Figure 6A). The residues that were observed as pairs of peaks with similar ^{1}H and ^{15}N chemical shifts in the 2D $^{1}H-^{15}N$ HSQC included Glu^{64}, Leu^{76}, Thr^{77}, Trp^{95}, Cys^{96}, Thr^{100}, Arg^{155}, and Cys^{160}. In addition, the residues forming the pairs of peaks are very close to two conserved cysteines (Cys^{96} and Cys^{159}) that are believed to be critical for the enzymatic activity of MerB (Figure 6B). The region of the structure mapped by the chemical shift changes (Figure 6A) can be considered as the Hg/DTT binding pocket on MerB, whereas the region mapped by the pairs of peaks highlights the binding pocket for the DTT moiety (Figure 6B). Both of the proposed binding pockets are larger than either DTT or Hg/DTT. Therefore, the chemical shifts observed between the free MerB and the MerB/DTT complex must be the result of other factors in addition to their proximity to either DTT or Hg/DTT. The pairs of peaks observed for several signals have to be directly related to DTT and the result of differences between the two diastereomers. These differences could be explained partly from a different orientation of the Hg/DTT in the binding pocket, but again, given the large area of the proposed binding pockets, other factors other than proximity must play a role in the differences between the two diastereomers. Although there are several possible explanations as to why the inferred binding pockets are larger than their ligands (Hg and DTT), there is a possibility for increased stability at and around the active site when these ligands are bound. Indeed, we have evidence that the region around Cys^{96} and Cys^{159} is stabilized by the binding of mercury (*61*). Cys^{96}, which is not observed in the spectra of the free form, is clearly observed in the MerB/Hg/DTT complex. In fact, Cys^{96} is bound directly to Hg(II) in the complex. The evidence for the binding of Hg(II) to Cys^{96} is based on the unusual chemical shift of the C^{β} (*61*).

Prediction of a Potential Hydrocarbon-Binding Pocket. Using the CAST server (http://cast.engr.uic.edu/cast) for the identification of structural pockets and cavities (*62*), the NMR structure of MerB was analyzed for the presence of a hydrophobic pocket that was large enough to accommodate the hydrocarbon moiety of organomercurial substrates. The program calculated that the side chains of many residues, mainly hydrophobic, spanning from the amino-terminal region to the carboxyl terminus, define a wide and deep cleft accessible to the solvent or to the potential substrates. On one side of this large pocket are localized the residues (Glu^{64}, Leu^{76}, Thr^{77}, Trp^{95}, Cys^{96}, Thr^{100}, Arg^{155}, and Cys^{160}) that bind the DTT moiety of the Hg−DTT, whereas on the opposite site, residues in the regions 97−115, 126−133,

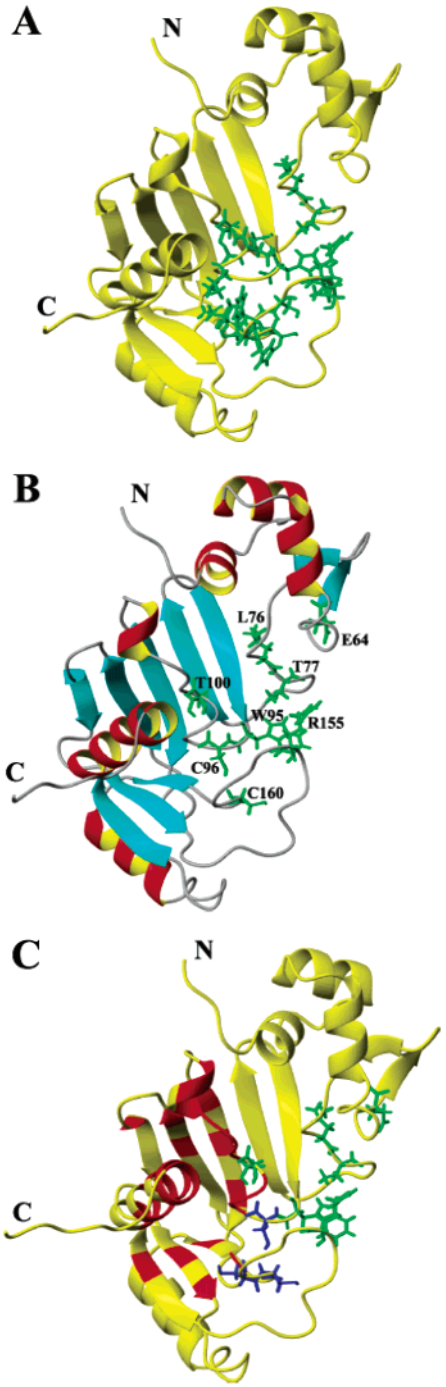

FIGURE 6: (A) Amino acids showing a significant chemical shift change $\{\Delta\delta_{ppm} > 0.2$, where $\Delta\delta_{ppm} = [(0.17\Delta N_{H(ppm)})^2 + (0.39\Delta C_{ppm})^2 + (\Delta H_{N(ppm)})^2]^{1/2}$ (*63*)$\}$ upon formation of the MerB/Hg/DTT complex, mapped onto a ribbon model of the NMR structure of MerB (yellow). The significantly shifted residues are shown in green, and they define the Hg/DTT binding site. (B) Ribbon model of MerB defining the binding site for the DTT moiety in the MerB/Hg/DTT complex. In green are shown the side chains of the residues that appear as doublets (Glu^{64}, Leu^{76}, Thr^{77}, Trp^{95}, Cys^{96}, Thr^{100}, Arg^{155}, and Cys^{160}) in the 2D $^{1}H-^{15}N$ HSQC spectrum of the MerB/Hg/DTT complex with racemic DTT (see text for details). (C) Ribbon model of MerB showing a potential organomercurial-binding site on the enzyme. All of the residues that form a wide cleft accessible to the solvent or to the hydrocarbon moiety of a potential organomercurial substrate are highlighted in red. The three solvent-exposed cysteines (Cys^{96}, Cys^{159}, and Cys^{160}) are colored in blue, and all other noncysteine residues that appear as doublets (Glu^{64}, Leu^{76}, Thr^{77}, Trp^{95}, Thr^{100}, and Arg^{155}) are shown in green.

143−145, 162−164, and 187−204 define a contiguous hydrophobic patch, positioned adjacent to Cys^{96} and Cys^{159} and large enough to accommodate a large aromatic group such as the one present in substrates like mersalyl (Figure 6C). Therefore, we propose that this hydrophobic pocket, present in MerB, binds the hydrocarbon moiety of the organomercurial substrate, and it is structured so that it is able to accommodate a diverse range of potential organomercurial substrates.

CONCLUSIONS

In this paper, NMR spectroscopy has been used to characterize the 3D solution structure of the organomercurial lyase MerB and its interaction with organomercurial substrates. MerB adopts a novel fold characterized by three separate antiparallel β-sheets surrounded by six α-helices. Comparison of the NMR-derived structure of MerB with known structures in the database failed to identify homologous folding patterns. This is not surprising given the unusual mechanism of this enzyme.

The knowledge of the 3D fold of MerB has provided insights into the role of the four cysteines in the protein sequence, all of which have been shown to be crucial for enzymatic activity (*21*, *22*). The highly conserved Cys^{117} plays a structural role as previously suggested (*22*). The remaining three cysteines (Cys^{96}, Cys^{159}, and Cys^{160}) are very close in space, they are all located in less well-defined loop regions of the protein structure, and they are all solvent accessible. These cysteine-containing regions appear to be part of the active site, and the intrinsic flexibility of these regions could at least partially account for the broad substrate specificity of MerB. In fact, a flexible binding site would allow the enzyme to easily accommodate a broad variety of substrates both aliphatic and aromatic, and this is the case for MerB.

We have also compared the NMR chemical shift resonances for free MerB and a MerB/Hg/DTT complex. This comparison has led to the identification of a set of residues that are part of the Hg/DTT binding site on MerB. These residues are close in space, and they cluster around the two highly conserved cysteines (Cys^{96} and Cys^{159}) that have been shown to play a crucial role in the catalytic activity of the enzyme (*21*, *22*). In addition, a detailed analysis of the NMR-derived 3D structure of MerB revealed the presence of a large hydrophobic pocket that could accommodate the hydrocarbon moiety of various substrates. Importantly, this hydrophobic pocket is located adjacent to the Hg/DTT binding site in the MerB structure. The elucidation of the structural features of MerB presented in this study will be extremely helpful in the ongoing attempts to exploit the potential of MerA and MerB in the bioremediation of organomercurial compounds.

ACKNOWLEDGMENT

We thank Jim Prestegard and Catherine Bougault for helpful discussions on the interpretation of the RDC data, Nico Tjandra for many useful comments, and Bao D. Nguyen for help and suggestions on several aspects of this investigation. We thank Frank Delaglio, Bruce Johnson, and Daniel Garrett for supplying the programs for NMR data processing and analysis and Lewis Kay and Wing-Yiu Choy for kindly providing NMR pulse sequences and a modified version of CNS. P.D.L. thanks Professor B. Di Blasio for encouraging her to undertake these studies.

REFERENCES

1. Munthe, J. (1992) The aqueous oxidation of elemental mercury by ozone, *Atmos. Environ. 26*, 1461−1468.
2. Pleijel, K., and Munthe, J. (1995) Modelling the atmospheric mercury cycle−chemistry in fog droplets, *Atmos. Environ. 29*, 1441−1457.
3. Mason, R., and Fitzgerald, W. (1996) The global mercury cycle: Oceanic and anthropogenic aspects, in *Global and Regional Mercury Cycles: Sources, Fluxes and Mass Balances* (Baeyens, W., Ed.) pp 85−108, Kluwer Academic, Dordrecht.
4. Choy, S. C., and Bartha, R. (1993) Cobalamin-mediated mercury methylation by *Desulfovibrio desulfuricans* LS, *Appl. Environ. Microbiol. 59*, 290−295.
5. Choy, S. C., Chase, J. T., and Bartha, R. (1994) Metabolic pathways leading to mercury methylation by *Desulfovibrio desulfuricans* LS, *Appl. Environ. Microbiol. 60*, 4072−4077.
6. Lindberg, S., Stokes, P., Goldberg, E., and Wren, C. (1987) Group report: Mercury. in *Lead, Mercury, Cadmium and Arsenic in the Environment* (Hutchinson, T. W., and Meema, K. M., Eds.) pp 17−34, John Wiley & Sons, New York, Chichester, Brisbane, Toronto.
7. Morel, F. M. M., Kraepiel, A. M. L., and Amyot, M. (1998) The chemical cycle and bioaccumulation of mercury, *Annu. Rev. Ecol. Syst. 29*, 543−566.
8. Kershaw, T. G., Clarkson, T. W., and Dhahir, P. H. (1980) The relationship between blood-brain levels and dose of methylmercury in man, *Arch. Environ. Health 35*, 28−36.
9. Kerper, L. E., Ballatori, N., and Clarkson, T. W. (1992) Methylmercury transport across the blood-brain barrier by amino acid carrier, *Am. J. Physiol. 265*, R761−R765.
10. Clarkson, T. W. (1997) The toxicology of mercury, *Crit. Rev. Clin. Lab. Sci. 34*, 269−403.
11. Sarafian, T., and Verity, M. A. (1991) Oxidative mechanisms underlying methylmercury neurotoxicity, *Int. J. Dev. Neurosci. 9*, 147−153.
12. Atchison, W. D., and Hare, M. F. (1994) Mechanisms of methylmercury-induced neurotoxicity, *FASEB J. 8*, 622−629.
13. Yoshino, Y., Mozai, T., and Nakao, K. (1966) Biochemical changes in the brain in rats poisoned with an alkyl mercuric compound, with special reference to the inhibition of protein synthesis in brain cortex slice, *J. Neurochem. 13*, 1223−1230.
14. Walsh, C. T., Distefano, M. D., Moore, M. J., Shewchuk, L. M., and Verdine, G. L. (1988) Molecular basis of bacterial resistance to organomercurial and inorganic mercuric salts, *FASEB J. 2*, 124−130.
15. Barkay, T., Miller, S. M., and Summers, A. O. (2003) Bacterial mercury resistance from atoms to ecosystems, *FEMS Microbiol. Rev. 27*, 355−384.
16. Hamlett, N. V., Landale, E. C., Davis, B. H., and Summers, A. O. (1992) Role of the Tn21 merT, merP and merC gene products in mercury resistance and mercury binding, *J. Bacteriol. 174*, 6377−6385.
17. Steele, R. A., and Opella, S. J. (1997) Structures of the reduced and mercury-bound forms of MerP, the periplasmic protein from the bacterial mercury detoxification system, *Biochemistry 36*, 6885−6895.
18. Fox, B., and Walsh, C. (1982) Mercuric reductase: purification and characterization of a transposon-encoded flavoprotein containing an oxidation−reduction-active disulfide, *J. Biol. Chem. 257*, 2498−2503.
19. Miller, S. (1999) Bacterial detoxification of Hg(II) and organomercurials, *Essays Biochem. 34*, 17−30.
20. Begley, T. P., Walts, A. E., and Walsh, C. T. (1986) Bacterial organomercurial lyase: overproduction, isolation and characterization, *Biochemistry 25*, 7186−7192.
21. Begley, T. P., Walts, A. E., and Walsh, C. T. (1986) Mechanistic studies of a protonolytic organomercurial cleaving enzyme: bacterial organomercurial lyase, *Biochemistry 25*, 7192−7200.
22. Pitts, K. E., and Summers, A. O. (2002) The roles of thiols in the bacterial organomercurial lyase (MerB), *Biochemistry 41*, 10287−10296.
23. Ogawa, H. I., Tolle, C. L., and Summers, A. O. (1984) Physical and genetic-map of the organomercury resistance (omr) and inorganic mercury resistance (hgr) loci of the incm plasmid r831b, *Gene 32*, 311−320.

24. Hansen, M. R., Mueller, L., and Pardi, A. (1998) Tunable alignment of macromolecules by filamentous phage yields dipolar coupling interactions, *Nat. Struct. Biol. 5* (12), 1065−1074.
25. Kay, L. E., Keifer, P., and Saarinen, T. (1992) Pure absorption gradient enhanced heteronuclear single quantum correlation spectroscopy with improved sensitivity, *J. Am. Chem. Soc. 114*, 10663−10665.
26. Shaka, A. J., Keeler, J., Frenkiel, T., and Freeman, R. (1983) An improved sequence for broadband decoupling: WALTZ-16, *J. Magn. Reson. 52*, 335−338.
27. Shaka, A. J., Barker, P. B., and Freeman, R. (1985) Computer-optimized decoupling scheme for wideband applications and low-level operation, *J. Magn. Reson. 64*, 547−552.
28. Piotto, M., Saudek, V., and Sklenár, V. (1992) Gradient-tailored excitation for single-quantum NMR spectroscopy of aqueous solutions, *J. Biomol. NMR 2*, 661−665.
29. Grzesiek, S., and Bax, A. (1993) The importance of not saturating water in protein NMR. Application to sensitivity enhancement and NOE measurements, *J. Am. Chem. Soc. 115*, 12593−12594.
30. Di Lello, P., Benison G. C., Omichinski, J. G., and Legault, P. (2004) Letter to the Editor: ^{1}H, ^{15}N, and ^{13}C resonance assignment of the 23 kDa organomercurial lyase MerB in its free and mercury-bound forms, *J. Biomol. NMR*, In press.
31. Marion, D., Kay, L. E., Sparks, S. W., Torchia, D. A., and Bax, A. (1989) Three-dimensional heteronuclear NMR of nitrogen-15 labeled proteins, *J. Am. Chem. Soc. 111*, 1515−1517.
32. Marion, D., Driscoll, P. C., Kay, L. E., Wingfield, P. T., Bax, A., Gronenborn, A. M., and Clore, G. M. (1989) Overcoming the overlap problem in the assignment of proton NMR spectra of larger proteins by use of a three-dimensional heteronuclear proton-nitrogen-15 Hartmann−Hahn multiple quantum coherence and nuclear Overhauser multiple quantum coherence spectroscopy: application to interleukin 1β. *Biochemistry 28*, 6150−6156.
33. Zuiderweg, E. R. P., McIntosh, L. P., Dahlquist, F. W., and Fesik, S. W. (1990) Three-dimensional ^{13}C-resolved proton NOE spectroscopy of uniformly ^{13}C-labeled proteins for the NMR assignment and structure determination of larger molecules, *J. Magn Reson. 86*, 210−216.
34. Kay, L. E., Clore, G. M., Bax, A., and Gronenborn, A. M. (1990) Four-dimensional heteronuclear triple-resonance NMR spectroscopy of interleukin-1β in solution. *Science 249*, 411−414.
35. Vuister, G. W., Clore, G. M., Gronenborn, A. M., Powers, R., Garrett, D. S., Tschudin, R., and Bax, A. (1993) Increased resolution and improved spectral quality in 4-dimensional ^{13}C-^{13}C separated HMQC−NOESY−HMQC spectra using pulsed-field gradients, *J. Magn Reson. Ser. B 101*, 210−213.
36. Vuister, G. W., and Bax, A. (1993) Quantitative *J* correlation: a new approach for measuring homonuclear three-bond $J(H^{N}H^{\alpha})$ coupling constants in ^{15}N-enriched proteins, *J. Am Chem. Soc. 115*, 7772−7777.
37. Farrow, N. A., Muhandiram, R., Pawson, A. U., Forman-Kay, J. D., and Kay, L. E. (1994) Backbone dynamics of a free and a phosphopeptide-complexed src homology 2 domain studied by ^{15}N NMR relaxation, *Biochemistry 33*, 5984−6003.
38. Ottinger, M., Delaglio, F., and Bax, A. (1998) Measurement of *J* and dipolar couplings from simplified two-dimensional NMR spectra, *J. Magn. Reson. 131*, 373−378.
39. Yang, D., Venters, R. A., Mueller, G. A., Choy, W. Y., and Kay, L. E. (1999) TROSY-based HNCO pulse sequences for the measurement of ^{1}HN-^{15}N, ^{15}N-^{13}CO, ^{1}HN-^{13}CO, ^{13}CO-^{13}C$^{\alpha}$ and ^{1}HN-^{13}C$^{\alpha}$ dipolar couplings in ^{15}N, ^{13}C, ^{2}H-labeled proteins, *J. Biomol. NMR 14*, 333−343.
40. Bax, A., Kontaxis, G., and Tjandra, N. (2001) Dipolar couplings in macromolecular structure determination, *Methods Enzymol. 339*, 127−174.
41. Delaglio, F., Grzesiek, S., Vuister, G. W., Zhu, G., Pfeifer, J., and Bax, A. (1995) NMRPipe- A multidimensional spectral processing system based on Unix pipes, *J. Biomol. NMR 6*, 277−193.
42. Garrett, D. S., Powers, R., Gronenborn, A. M., and Clore, G. M. (1991) A common sense approach to peak-peaking in 2-dimensional, 3-dimensional and 4-dimensional spectra using automatic computer analysis of contour diagrams, *J. Magn. Reson. 95*, 214−220.
43. Johnson, B. A., and Blevins, R. A. (1994) NMRView- A computer program for the visualization and analysis of NMR data, *J. Biomol. NMR 4*, 603−614.
44. Fletcher, C. M., Jones, D. N. M., Diamond, R., and Neuhaus, D. (1996) Treatment of NOE constraints involving equivalent or nonstereoassigned protons in calculations of biomacromolecular structures, *J. Biomol. NMR 8*, 292−310.
45. Cornilescu, G., Delaglio, F., and Bax, A. (1999) Protein backbone angle restraints from searching a database for chemical shift and sequence homology, *J. Biomol. NMR 13*, 289−302.
46. Bystrov, V. F. (1976) Spin−spin coupling and the conformational states of peptide systems, *Prog. NMR Spectrosc. 10*, 41−81.
47. Wishart, D. S., Sykes, B. D., and Richards, F. M. (1992) The chemical-shift index: a fast and simple method for the assignment of protein secondary structure through NMR spectroscopy, *Biochemistry 31*, 1647−1651.
48. Wishart, D. S., and Sykes, B. D. (1994) The ^{13}C chemical-shift index: a simple method for the identification of protein secondary structure using ^{13}C chemical-shift data, *J. Biomol. NMR 4*, 171−180.
49. Gagné, S. M., Tsuda, S., Li, M. X., Chandra, M., Smillie, L. B., and Sykes, B. D. (1994) Quantification of calcium-induced secondary structural changes in regulatory domain of troponin-C, *Protein Sci. 3*, 1961−1974.
50. Warren, J. J., and Moore, P. B. (2001) A maximum likelihood method for determining D_a^{PQ} and R for sets of dipolar coupling data, *J. Magn. Reson. 149*, 271−275.
51. Clore, G. M., Gronenborn, A. M., and Tjandra, N. (1998) Direct structure refinement against residual dipolar couplings in the presence of rhombicity of unknown magnitude, *J. Magn. Reson. 131*, 159−162.
52. Brunger, A. T., Adams, P. D., Clore, G. M., Gros, P., Grosse-Kunstleve, R. W., Jiang, J. S., Kuszewski, J., Nilges, M., Pannu, N. S., Read, R. J., Rice, L. M., Simonson, T., and Warren, G. L. (1998) Crystallography and NMR system (CNS): A new software system for macromolecular structure determination, *Acta Crystallogr. D54*, 905−921.
53. Stein, E. G., Rice, L. M., and Brünger, A. T. (1997) Torsion-angle molecular dynamics as a new efficient tool for NMR structure calculation, *J. Magn. Reson. 124*, 154−164.
54. Choy, W. Y., Tollinger, M., Muller, G. A., and Kay, L. E. (2001) Direct structure refinement of high molecular weight proteins against residual dipolar couplings and carbonyl chemical shift changes upon alignment: an application to maltose binding protein, *J. Biomol. NMR 21*, 31−40.
55. Laskowski, R. A., Rullmann, J. A. C., Macarthur, M. W., Kaptein, R., and Thornton, J. M. (1996) ACQUA and PROCHECK−NMR: Programs for checking the quality of protein structures solved by NMR, *J. Biomol. NMR 8*, 477−486.
56. Korandi, R., Billeter, M., and Wüthrich, K. (1996) MOLMOL: a program for display and analysis of macromolecular structures, *J. Mol. Graphics 14*, 51−55.
57. Hutchinson, E. G., and Thornton, J. M. (1996) PROMOTIF − a program to identify and analyze structural motifs in proteins, *Protein Sci. 5*, 212−220.
58. Holm, L., and Sander, C. (1993) Protein structure comparison by alignment of distance matrices, *J. Mol. Biol. 233*, 123−138.
59. Gajiwala, K. S., and Burley S. K. (2000) Winged helix proteins, *Curr. Opin. Struct. Biol. 10*, 110−116.
60. Moore, M. J., Distefano, M. D., Zydowsky, L. D., Cummings, R. T., and Walsh, C. T. (1990) Organomercurial lyase and mercuric ion reductase: nature's mercury detoxification catalysts, *Acc. Chem. Res. 23*, 301−308.
61. Benison, G. C., Di Lello, P., Shokes, J. E., Cosper, N. J., Scott, R. A., Legault, P., and Omichinski, J. G. A stable mercury-containing complex of the organomercurial lyase MerB: Catalysis, product release and direct transfer to MerA, *Biochemistry 43*, 8333−8345.
62. Liang, J., Edelsbrunner, H., and Woodward, C. (1998) Anatomy of protein pockets and cavities: measurement of binding site geometry and implications for ligand design, *Protein Sci. 7*, 1884−1897.
63. Farmer, B. T., Constantine, K. L., Goldfarb, V., Friedrichs, M. S., Wittekind, M., Yanchunas, J., Robertson, J. G., and Mueller, L. (1996) Localizing the $NADP^{+}$ binding site on the MurB enzyme by NMR, *Nat. Struct. Biol. 3*, 995−997.

BI049669Z